

Detection and Segmentation of Colonic Polyps on Implicit Isosurfaces by Second Principal Curvature Flow

Cees van Wijk*, Vincent F. van Ravesteijn, Frans M. Vos, and Lucas J. van Vliet, *Member, IEEE*

Abstract—Today’s computer aided detection systems for computed tomography colonography (CTC) enable automated detection and segmentation of colorectal polyps. We present a paradigm shift by proposing a method that measures the amount of protrudeness of a candidate object in a scale adaptive fashion. One of the main results is that the performance of the candidate detection depends only on one parameter, the amount of protrusion. Additionally the method yields correct polyp segmentation without the need of an additional segmentation step. The supervised pattern recognition involves a clear distinction between size related features and features related to shape or intensity. A Mahalanobis transformation of the latter facilitates ranking of the objects using a logistic classifier. We evaluate two implementations of the method on 84 patients with a total of 57 polyps larger than or equal to 6 mm. We obtained a performance of 95% sensitivity at four false positives per scan for polyps larger than or equal to 6 mm.

Index Terms—Biomedical image processing, image analysis, partial differential equation (PDE), polyp detection, surface evolution.

I. INTRODUCTION

PROTRUSIONS of a surface embedded in a 3-D image are difficult to detect. The challenge increases even further if the surface itself is highly structured and interacts with the protruding elements. Such a problem is the detection of polyps in computed tomography (CT) colonography (CTC), a minimal invasive technique for examining the colon surface (cf. Fig. 1). There is an increasing interest in computer aided detection (CAD) systems for polyp detection in CTC data to assist the radiologist [1]–[7]. Such a CAD system typically consists of three consecutive steps: colon segmentation; detection of polyp candidates; and supervised classification of candidates as polyps or nonpolyps [8], [9].

Adenomatous polyps are important precursors to colon cancer and develop due to genetic mutations in the mucosa

Manuscript received May 26, 2009; revised August 12, 2009; accepted August 15, 2009. Current version published March 03, 2010. *Asterisk indicates corresponding author.*

*C. van Wijk is with the Quantitative Imaging Group, Delft University of Technology, NL-2628 CJ Delft, The Netherlands.

V. F. van Ravesteijn and L. J. van Vliet are with the Quantitative Imaging Group, Delft University of Technology, NL-2628 CJ Delft, The Netherlands (e-mail: l.j.vanvliet@tudelft.nl).

F. M. Vos is with the Quantitative Imaging Group, Delft University of Technology, NL-2628 CJ Delft, The Netherlands and also with the Department of Radiology, Academic Medical Center, NL-1100 DD Amsterdam, The Netherlands (e-mail: f.m.vos@tudelft.nl).

Color versions of one or more of the figures in this paper are available online at <http://ieeexplore.ieee.org>.

Digital Object Identifier 10.1109/TMI.2009.2031323

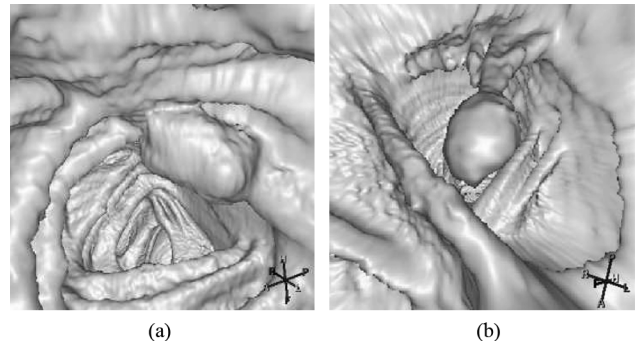


Fig. 1. Isosurface renderings (at -650 HU) of the colon surface showing typical polyps in their structured surroundings.

cells [10]. This process of oncogenesis leads to enhanced cell proliferation causing the polyp to grow and to evolve from a small adenoma into a large adenoma into a carcinoma. This induces a morphological change to the colon surface,¹ that manifests itself as tissue protruding into the lumen. The deformation is an important property which is used in the detection by radiologists as well as gastroenterologists.

Practically all CAD systems for polyp detection analyze the local curvature of the colon surface, which is subsequently used to compute shape descriptors such as shape index or curvedness [13], [14]. Computation of the curvature values is typically done in “one shot” on a single predetermined scale, which is defined as the effective size of the area over which the image features are calculated. We will maintain this definition throughout the paper.

We propose a new paradigm for the detection and segmentation of polyps that effectively copes with the highly structured environment. The novelty of the approach is in computing an intensity change field, which removes protruding elements from the underlying data, while leaving the highly structured folds intact. The deformation algorithm is described by a partial differential equation (PDE) that is steered by the second principal curvature.

In order to demonstrate the method’s efficiency, we make use of a pattern recognition system introduced by us in [15]. The paper involved polyp detection based on the explicit representation of the colon surface. The method proved to generalize well and lead to satisfying results. It encouraged us to further investigate the candidate detection system. Presently, we propose a

¹Not all colonic lesions grow into protruding polyps. It is estimated that approximately 10% of the lesions are so-called flat adenomas [11], [12].

technique based on an implicit representation of the colon surface, which enables a number of improvements over the explicit model. A concise description of the classifier is contained, since it is only indirectly related to the paper's main objective. This allows us to fully go into all facets associated with second principal curvature flow.

A. Previous Work

For the detection of candidate regions, Summers *et al.* [13] proposed to use the mean and Gaussian curvature. They were computed by methods from differential geometry, by fitting a fourth-order B -spline to local 5-mm-radius neighborhoods of a triangulated isosurface [16]. Candidates were generated by selecting a range of mean and Gaussian curvature values. Additionally, a large number of other shape criteria were used [17, Table 2], to limit the number of false positive detections. Similarly, Yoshida *et al.* [14] used the shape index and curvedness to find candidate objects on the colon surface. The shape index SI and curvedness CV are functions of the principal curvatures of the surface

$$SI = \frac{1}{2} - \frac{1}{\pi} \arctan \left(\frac{\kappa_1 + \kappa_2}{\kappa_1 - \kappa_2} \right)$$

$$CV = \sqrt{\frac{\kappa_1^2 + \kappa_2^2}{2}} \quad (1)$$

with κ_1 and κ_2 the maximum and minimum principal curvature respectively. A Gaussian-shaped window (aperture) of fixed size was used to compute the curvatures from the 3-D CT data.

Alternatively, Kiss *et al.* [3] proposed to use a sphere fitting method to generate candidates. The colon surface was classified as convex depending on the side on which the center of the fitted sphere was found (in tissue or in air). This method classifies roughly 90% of the colon surface as concave, that is as "normal." To the remaining part of the colon surface a generalized Hough transformation was applied using a spherical model. Candidate objects were generated by finding local maxima in the parameter space created by the Hough transformation.

Konukoglu *et al.* [1], [18] proposed a method that is in some sense the inverse of the approach that is proposed in the current paper. Effectively, a wall evolution algorithm is described based on a level-set formulation that regularizes and enhances polyps as a preprocessing step to CTC CAD algorithms. The underlying idea is to evolve the polyps towards spherical protrusions on the colon wall while keeping other structures, such as haustral folds, relatively unchanged. Thereby, the performance of CTC CAD algorithms is potentially improved, especially for smaller polyps.

Conventionally, the shape-based candidate detection methods [1], [2], [13], [14], [19], [20] apply several conservative thresholds to the mean curvature, principal curvatures, sphericity ratio and/or shape index to generate candidate regions.

B. Problem Definition

We identify a number of challenges that are associated with the detection of polyp candidates. First, optimization of the parameters is always complicated by the limited availability of training examples. This may lead to overtraining for a specific patient population, patient preparation, scanning hardware or

scanning protocol. Thus, it is preferred to keep the number of restrictive criteria to a minimum.

Second, to achieve good discrimination power and accurate measurement [21] of lesion size, precise "delineation" (or segmentation) of the candidate is needed. Although a number of methods are available for segmentation purposes [17], [22], [23], adding such a separate step would introduce more parameters to the CAD pipeline and should be avoided. Fuzzy segmentation methods using sophisticated pattern recognition techniques might preclude this problem.

A third challenge is associated with the computation of the first and second order derivatives, which are needed to compute the principal curvatures and to characterize local shape. The derivative operators must act on a range of sizes and should not have optimal performance for a specific size only. Ideally, the scale should adapt to the underlying image structure. To our knowledge no research has been performed to either analyze the effect of scale or to determine the optimal scale for polyp detection. It is partly addressed in [24] by performing the curvature computation on a high resolution triangulated isosurface mesh thereby limiting the low pass filtering across the isosurface. Furthermore, some research on scale selection for CTC in general has been performed in [25] and [26].

Last, detecting large polyps is (clinically) more important than detecting smaller ones. One would like to have this built into the CAD system. In other words, the detection method must perform optimal for large polyps.

A steadily growing number of papers [7], [14], [27]–[31] report on the performance of specific polyp detection algorithms. Unfortunately, a proper comparison of algorithms is complex due to differences in prevalence, patient preparation, scanning protocol, and determination of the ground truth.

We aim to convey some general requirements for polyp detection systems.

- 1) It should not involve many parameters which need to be tuned in the presence of a limited number of polyps.
- 2) A separate segmentation step should be avoided as it might add more parameters.
- 3) It must be able to cope with the whole polyp size range encountered in practice. and
- 4) It should take into account the increased clinical relevance of larger polyps.

C. Objective

We aim to introduce a new paradigm for the detection of protruding regions on highly structured surfaces embedded in a 3-D image. Polyps are assumed to have introduced a deformation to the original (healthy) colon surface. We will describe a novel method to reconstruct the data without these protrusions. Effectively, the technique aims to "undo" the deformation by modifying the underlying intensities so that the protruding shape is no longer there.

The proposed method does not require any assumptions on the lesion shape such as axial-symmetry, sphericity or lesion size, other than that it protrudes. It works well for highly irregular protruding objects. Lesion candidates are generated using only a single threshold. Small variations of the threshold affect the detection sensitivity of the smaller polyps first. Additionally,

the resulting segmentations include the complete object (both head and neck).

In earlier work [32], we proposed a scheme that operated on an explicit representation of the colon surface, which was obtained by a triangulation of the isosurface at -650 HU. Only information of this particular isophote was used to estimate the structured surface without the protrusions. Any (beneficial) information from isophotes with higher or lower intensities was ignored. The scheme proposed in this paper differs fundamentally by acting on an implicit representation of the colon surface. That is, it uses information from other isophotes as well. Consequently, there is no need for tuning (optimizing) the intensity level of the isosurface. Another advantage of this method is that topological complexities and complex mesh processing tasks, such as mesh generation and mesh smoothing, are avoided. We will compare both methods and demonstrate that the two techniques are to some extent complementary. Moreover, exploiting the complementary aspects will be shown to lead to improved sensitivity.

II. METHODOLOGY

A. Materials

A total of 84 patients with an increased risk for colorectal cancer were consecutively included in a previous study [33]. All data were acquired using a $M \times 8000$ multislice CT scanner (Philips Healthcare, Best, The Netherlands) using the same scanning protocol for all scans (120 kV, 100 mAs, 4×2.5 mm collimation, pitch 1.25, standard reconstruction filter). Slice thickness was 3.2 mm. All patients adhered to an extensive laxative regime without taking a tagging agent with their diet. All patients underwent CT colonography before colonoscopy. The patients were scanned in both prone and supine position; thus, a total of 168 scans were used in our study. The findings of colonoscopy served as the golden standard. Polyp size was also measured during colonoscopy by comparison with an open biopsy forceps of known size. A research fellow annotated the location of polyps in all CT scans. For the 84 patients, 108 polyps were annotated. The number of polyps with a size larger than or equal to 6 mm was 57 and the number of polyps larger than or equal to 10 mm was 32. Fig. 2 shows a histogram of the optical colonoscopy size-measurements. Conventionally, polyps which are smaller than 6 mm are considered clinically unimportant. Therefore, they were not used in the performance analysis. The peak at 10 mm polyp size is caused by the fact that in clinical practice only a few bins are used: smaller than 6 mm, between 6 and 10 mm and larger than or equal to 10 mm.

Experts labelled the polyps in CT data based on the optical colonoscopy findings without using CAD. A candidate generated by the CAD system was labelled as a true positive if an annotation was within 5 mm from any of the voxels in the candidate and was not closer to any other candidate. A margin of 5 mm was used to accommodate inaccurate localization by the expert. Especially for the explicit method, such a margin is needed to accommodate annotation inside the polyp. To be able to make a proper comparison between the two methods, the same margin is used for both techniques.

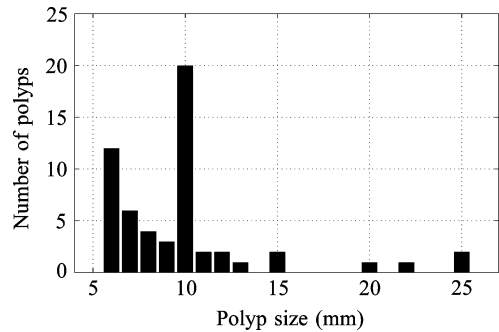


Fig. 2. Distribution of sizes obtained during colonoscopy of 57 polyps larger than or equal to 6 mm in 84 patients from a previous study [33]. One polyp of 45 mm is not visible in the histogram.

B. Method

A typical polypoid shape is shown in Fig. 3(a). Suppose that the points on the convex region of the polyp (the polyp head) are iteratively moved inwards. In effect this process will “flatten” the object [Fig. 3(c)]. Note that the convex region expands during the process and will ultimately include the polyp neck as well. After a certain amount of deformation, the surface flattening is such that the protrusion is completely removed. That is, the surface looks like as if the object was never there. This is the key concept on which the method is based.

Before formalizing on the operator we first have a closer look at the second order differential properties of the implicit surface embedded in a 3-D voxel space. The colon can be considered as a long elongated structured tube. For a perfect cylinder shape the principal curvatures are smaller than or equal to zero everywhere. However, the colon contains many folds, i.e., structures which are bended only in one direction: the first principal curvature is larger than zero, whereas, the second principal curvature is close to zero. Protruding objects, such as polyps, have positive values for the first and second principal curvature. Therefore, an operator is designed to affect only on points with a positive second principal curvature and in such a way that the second principal curvature decreases. Repeated application of the operator will eventually yield an image where the second principal curvature is smaller than or equal to zero everywhere.

Consider once more the schematic representation of a polyp in Fig. 3(a). The distinction between the head ($\kappa_1 > 0$, $\kappa_2 > 0$) and neck ($\kappa_1 > 0$, $\kappa_2 \leq 0$) regions of the object is made by the sign of the second principal curvature. On the line connecting the inflection points A and B in the figure (separating the regions “head” and “neck”) the Gaussian curvature is zero. The proposed method initially adapts the head region only. It will now be demonstrated that such adaptation leads to an expansion of this region.

To that end, Fig. 3(b) shows a planar cross section through A, spanned by the local gradient vector and the direction of the second principal curvature. Let us merely consider the curve emanating from this cross section. The steepness of this curve corresponds to its first derivative; the curvature corresponds to its second derivative and is given by

$$\kappa = -\frac{\Delta y}{|\nabla y|} \quad (2)$$

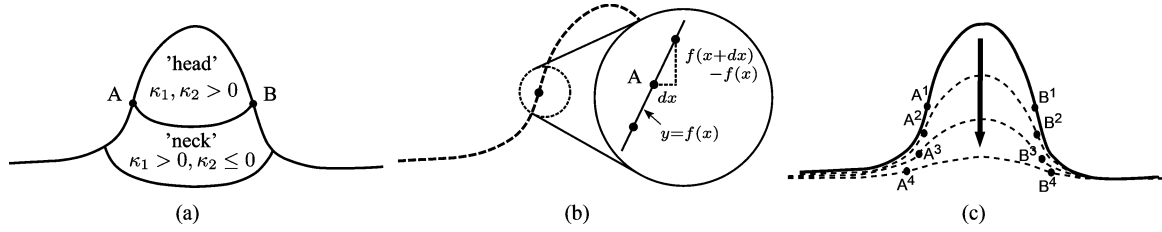


Fig. 3. Schematic illustration of the deformation process. (a) Three regions (head, neck and periphery) are distinguished. (b) Second principal curvature κ_2 is zero at the border between the head and neck region. (c) Head region expands during the deformation process.

in which Δy represents the second derivative of the curve. By convention κ has a sign opposite to that of the second derivative. Observe that this curvature is positive on the “head” side from A and negative on the “neck” side from A; the curvature equals zero in A. At the position of A the second derivative is

$$\Delta y = \frac{d^2 f}{dx^2} = \lim_{dx \rightarrow 0} \frac{\frac{f(x+dx) - f(x)}{dx} - \frac{f(x) - f(x-dx)}{dx}}{dx} = 0. \quad (3)$$

A reduction of the protrusion in the head region implies that the value of $f(x + dx)$ in (3) is lowered. Consequently, the second derivative in A (Δy) becomes negative, and the curvature (κ) positive. Thus, the zero crossing of the second derivative will shift outwards in Fig. 3(b) and the head region will expand into the neck region.

The effect of repeatedly reducing the protrusion is illustrated in Fig. 3(c). The points with zero second principal curvature shift from A^1 to A^4 and B^1 to B^4 . Eventually, the protrusion is flattened over the complete shape, i.e., both the head and neck regions. Although the initial delineation of the head region of the structure (in which the deformation is started) may be affected by noise, the area of operation eventually spreads to the entire polyp area. It is this property that makes the procedure robust. The results section contains some examples to illustrate the method’s efficacy.

C. Second Principal Curvature Flow

A scheme to remove protruding elements from a curve in 2-D is the Euclidean shortening flow [34]. A similar approach can be taken in 3-D, for which the flow is governed by

$$\frac{\partial I}{\partial t} = -g(\kappa_1, \kappa_2) |\nabla I| \quad (4)$$

with κ_1 and κ_2 the first and second principal curvatures, $|\nabla I|$ the gradient magnitude of the input image I , and $g(\cdot)$ a curvature dependent function characterizing the flow. The principal curvatures can be derived from the trace of the Hessian matrix H

$$H = \begin{bmatrix} I_{xx} & I_{xy} & I_{xz} \\ I_{yx} & I_{yy} & I_{yz} \\ I_{zx} & I_{zy} & I_{zz} \end{bmatrix} \quad (5)$$

with x, y and z the image coordinates and I_{ij} the second derivative $I_{ij} = \partial^2 I / \partial i \partial j$. In gauge coordinates the Hessian is a diagonal matrix with terms [35]: I_{gg} , I_{uu} , and I_{vv} . The first term is the second derivative in gradient direction; the second and third terms are the second derivatives in the directions of the principal

curvatures of the isosurface perpendicular to the gradient vector. The latter two relate to the principal curvatures of the isosurface

$$\begin{aligned} I_{uu} &= -\kappa_1 |\nabla I| \\ I_{vv} &= -\kappa_2 |\nabla I|. \end{aligned} \quad (6)$$

With the definition of inward normals, the second principal curvature in the colon is everywhere smaller than or equal to zero, except on protruding regions. Here, both the first and second principal curvatures are positive and the corresponding second derivatives are negative.

$g(\kappa_1, \kappa_2)$ may be defined in various ways [36], e.g., by the mean curvature [37], [38] or the Gaussian curvature. We require that $g(\kappa_1, \kappa_2)$ is continuous, especially at locations where the sign of κ_2 changes, to avoid a discontinuous deformation. Moreover, it must be small on folds with a small positive value of κ_2 so that the deformation on such locations is small. Reversely, the response to polyps with two large principal curvatures should be large. Accordingly, we solve the following nonlinear PDE:

$$\frac{\partial I}{\partial t} = \begin{cases} I_{vv} & (\kappa_2 > 0) \\ 0 & (\kappa_2 \leq 0). \end{cases} \quad (7)$$

Thus, only at protruding regions the image intensity is reduced by an amount proportional to the local second derivative in the direction of κ_2 .

D. Implementation

The proposed method is applied to voxels on and around the colon surface. This region of interest (ROI) is defined by a mask. First, a binary image is obtained by thresholding the CT image at -650 HU. Subsequently, the mask is generated by applying the exclusive or (XOR) operation to an eroded and a dilated version of the binary image. The number of iterations for the dilation and erosion should be such that the full air-colon transition is included in the resulting mask image. We used a conservative value of 10 mm for the radius of the erosion and dilation kernels.

The partial differential (7) is solved for the voxels in the ROI defined previously. The intensities of voxels outside the ROI are not altered and serve as Dirichlet boundary conditions. The left-hand side of (7) is discretized by a forward difference scheme

$$\frac{\partial I}{\partial t} = \frac{I^{t+1} - I^t}{dt} + O(dt). \quad (8)$$

The right-hand side of (7) requires computation of first and second order derivatives. The first order derivative is determined by the local orientation of the normal field. An accurate estimate is required to prevent diffusion of information across isophotes,

leading to blurry effects. Unfortunately, simple central difference derivative operators are known to have rather poor rotation invariance [39]. Therefore, the first and second order derivatives are computed after a (second-order) Taylor expansion in a $3 \times 3 \times 3$ neighborhood [40]. They are used to compute I_{vv} .

The image values are modified in a semi-implicit manner comparable to a Gauss-Seidel scheme, meaning that some of the underlying intensity values are at time $t + 1$, while others are at time t

$$I^{t+1} = \begin{cases} I^t + \frac{\Delta t}{(\Delta x)^2} I_{vv}^{t+1/2} & (\kappa_2 > 0) \\ I^t & (\kappa_2 \leq 0) \end{cases} \quad (9)$$

in which $I_{vv}^{t+1/2}$ indicates that it is computed with information from time steps t and $t + 1$. For Laplace's equation, numerical stability is guaranteed if the term $\Delta t / (\Delta x)^2$ is smaller than $1/6$ [41]. Therefore, the maximum time step for which stability is attained depends on the direction in which the voxel size is smallest (typically in-plane): $(\Delta t)_{\max} = 1/6 \cdot (\Delta x)^2$. Note that this is a conservative value since we only use the principal second derivative, I_{vv} , instead of the full Laplacian: $I_{gg} + I_{uu} + I_{vv}$. The aspects of stability, convergence and correctness for similar problems have been elaborately discussed in [34]. For a more formal discussion, see [42] and also [41]. In practice, we have never encountered a problem concerning the stability and convergence of the solution.

Summarizing, the algorithm acts only on the head regions in which $\kappa_2 > 0$. A new intensity is assigned by (9) to each voxel within such a region. Subsequently, the principal curvatures are recomputed. Some of the voxels which initially had zero or negative second principal curvature will now be in the head region and will be added to the area of operation. In this way, during iteration, the area of operation will expand from the head into the neck region.

An obvious stopping criterion would be to track the amount of intensity change during iterations and stop when the amount of intensity change at a particular iteration is lower than some predefined value. Unfortunately, this leads to an underestimate of the protrusion of large objects, with a low value for the second derivative even when the protrusion may be quite large. In our implementation, we have taken a heuristic approach. After each iteration, the number of voxels that are added to the convex region is counted. The algorithm stops when this number is zero.

A crucial property of the method is that the effective kernel scale increases with each iteration. Such adaptation occurs since the curvature calculation continuously uses the result from the previous step. In effect, the scale "adapts" to the underlying image structure, because a small protrusion will require less iterations to be flattened into the background than a large one. In other words, the effective scale varies locally as the number of iterations needed to reach a "steady state" differs from location to location. Simultaneously, the area of operation, which is delimited by zero second principal curvature, also changes during iterations. By definition, the head region of a structure is adapted first, but subsequently the area of operation extends to the neck region (see Fig. 3). Existing methods typically estimate curvature values in "one shot" by selecting one scale of derivative operators *a priori*. A limitation of the current method may be as-

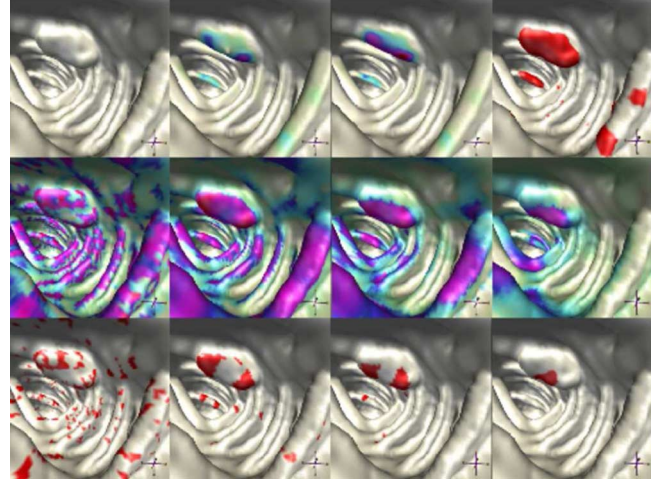


Fig. 4. Demonstration of polyp detection by the curvature flow (first row). The second and third row show results as obtained by thresholding the shape index, computed at different scales. See text for details.

sociated with protruding objects with small κ_2 . Such structures deform slowly due to small curvature. It will be demonstrated that the detection of large polyps is not hampered by this limitation (see Section III-B).

Fig. 4 demonstrates that the method works well also for highly irregular shapes. The first row shows the isosurface (rendered at -650 HU) at different stadia of the deformation process. During the first iterations only the two protruding regions on the left and right side of the polyp are affected. In later stages these two regions merge and also the middle part is deformed. The steady state solution and the resulting segmentation by thresholding is shown in the last two pictures of the first row. The second row shows the shape index (SI) computed from Gaussian derivatives obtained using different scales ($\sigma = 2, 4, 8, 12$ mm), red corresponds to $SI = 1$, magenta to $SI = 0.75$ (e.g., on folds). The third row shows the regions with SI larger than 0.8. The example demonstrates that scale has a profound effect on the resulting SI values. All polyps in our dataset that are larger than 10 mm have multiple separated head regions when "observed" at a small scale (see Fig. 11(b) for the performance of our algorithm on large objects).

E. Candidate Segmentation

The steady state yields new intensities for voxels, particularly in protruding regions. We will now demonstrate that the intensity change is a measure for the amount of displacement of the isosurface.

Let \vec{x} represent a position in which the intensity $I^{t=t_0}(\vec{x})$ is halfway the intensities of the colon lumen and the tissue. Furthermore, the algorithm is asserted to displace the isosurface through \vec{x} by a small amount δ [smaller than the width of the point spread function (PSF)] after some iterations at $t = t_i$. Then, the intensity $I^{t=t_i}(\vec{x})$ can be computed via a first-order Taylor series expansion

$$I^{t=t_i}(\vec{x}) = I^{t=t_0}(\vec{x}) + \delta \cdot \nabla I^{t=t_0}(\vec{x}) + \epsilon. \quad (10)$$

Notice that δ refers to a hypothetical step size corresponding to a small displacement of the isosurface. Reversely, a small change

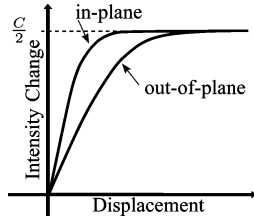


Fig. 5. Sketch of the relation between colon surface displacement and the observed intensity change for positions halfway the step edge. The relation depends on the apparent local scale of the PSF, i.e., the scale in the direction of the surface normal. Often, the scanner resolution is not isotropic: the in-plane resolution is larger than the out-of-plane resolution. As a consequence, the relation depends also on the direction of surface displacement.

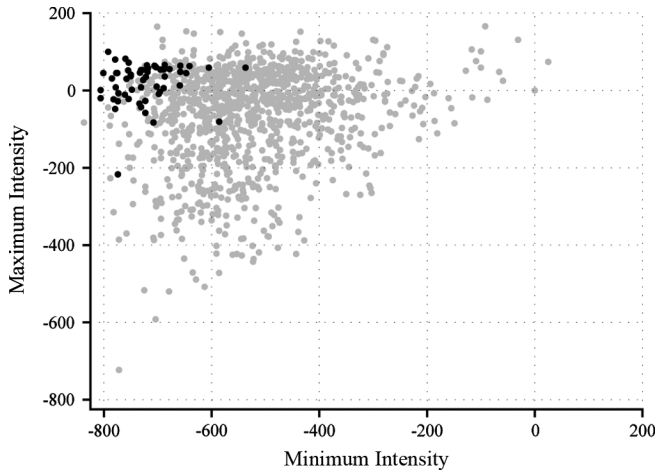


Fig. 6. Feature space of the maximum and minimum intensities for each candidate region. Annotated polyps are depicted by black dots and have maximum intensities around 0 HU (tissue) and minimum intensities around -650 HU. Only one in every 20 false positives is shown as a grey dot.

in intensity relates linearly to the amount of displacement. However, large displacements of the isosurface cannot be described as such. The intensity change levels off for displacements larger than the PSF width

$$I^{t=t_\infty}(\vec{x}) = I^{t=t_0}(\vec{x}) - \frac{C}{2} \quad (11)$$

in which C denotes the total contrast over the transition from lumen to tissue (typically around 1000 HU).

The sketch in Fig. 5 illustrates the relation between the intensity change (before and after deformation) and the colon surface displacement, halfway the air–tissue transition. Clearly, the intensity change is monotonically increasing with increasing displacement of the isosurface. This would permit a segmentation by a simple threshold on the intensity change if the data were isotropic, but unfortunately CT data often are not. The in-plane resolution is frequently higher than the resolution in scanning direction (z). In other words, the apparent scale of the PSF σ_{apparent} depends on the direction of the colon surface normal. Consequently, the relation between intensity change and colon surface displacement (cf. Fig. 5) depends on the orientation of the protruding structure. To solve this problem, the derivative kernels are made anisotropic such that the apparent scale will be isotropic and equal to a certain target scale σ_{target} . The kernel scale σ_i , in the direction $i \in \{x, y, z\}$, is computed by

$\sigma_i = \sqrt{\sigma_{\text{target}}^2 - \sigma_{\text{apparent},i}^2}$, in which $\sigma_{\text{apparent},i}$ is the apparent (anisotropic) scale of the PSF. Polyp candidate regions are segmented by thresholding the intensity change field, followed by a labelling operation. The threshold value is 100 HU corresponding to the threshold of 0.4 mm surface displacement as used in [32] for data with an assumed Gaussian PSF [43] with $\sigma = 1.6$ mm.²

F. Features for Classification

For each candidate object, five features are computed. These features relate to the two properties that are primarily used by a radiologist: shape of a candidate and intensity distribution inside a candidate. We explicitly make this distinction since only size descriptors permit a ranking of the candidate objects in a way that relates to clinical relevancy. Accordingly, size related features will be treated differently than the other features in the pattern recognition step. Conventionally, polyp size is defined as the single largest diameter, excluding the stalk. We compute it automatically using the method described in [23], which not only returns the largest diameter (LongAxis), but also the shortest diameter (ShortAxis). These are the first two size related features that are used in the classification. Notice that their ratio incorporates shape information. The third feature is the maximum intensity change (MaxIntChange) within each segmented region (candidate). It directly relates to the isosurface displacement (cf. Fig. 5). For larger polyps the values of this feature will be large and vice versa. The fourth and fifth features used for classification are the 5 and 95 percentile intensities inside the candidate. We employ these percentile values and not the minimum and maximum intensities to increase the robustness against noise. For simplicity, we will refer to these two features as the minimum (MinHU) and maximum (MaxHU) intensity values inside the objects. Notice that all features depend on the intensity change field since all are computed over the segmented volume of a candidate. Only the MaxIntChange feature is directly derived from the intensity change field in the segmented volume, the others are computed from the original CT data.

G. Classifier Training

It was mentioned previously that the intensity features do not (directly) allow for an ordering of the candidates. As an example, consider the feature space of MinHU and MaxHU shown in Fig. 6. The black dots denote true positive candidates and the grey dots denote false positive candidates.

The distribution of polyps is somewhat Gaussian, and there is a large overlap with the nonpolyps. The latter do not show a simple distribution in this space. For these reasons, these two features are not used *directly* for classifier training. Instead, we compute the Mahalanobis distance to the polyp class center. Such a mapping orders the candidates by the distance to the center of the Gaussian, i.e., the center of the polyp class yield zero Mahalanobis distance. Notice that the center and width of the Gaussian are to be determined on independent training data. This strategy mimics the use of a Gaussian one-class classifier

²Halfway the air–tissue transition: $\nabla I^{t=t_0} = C/\sigma\sqrt{2\pi} = 1000/1.6\sqrt{2\pi} \approx 250$ HU/mm, thus 100 HU \triangleq 0.4 mm, i.e., equal to the threshold used in [32].

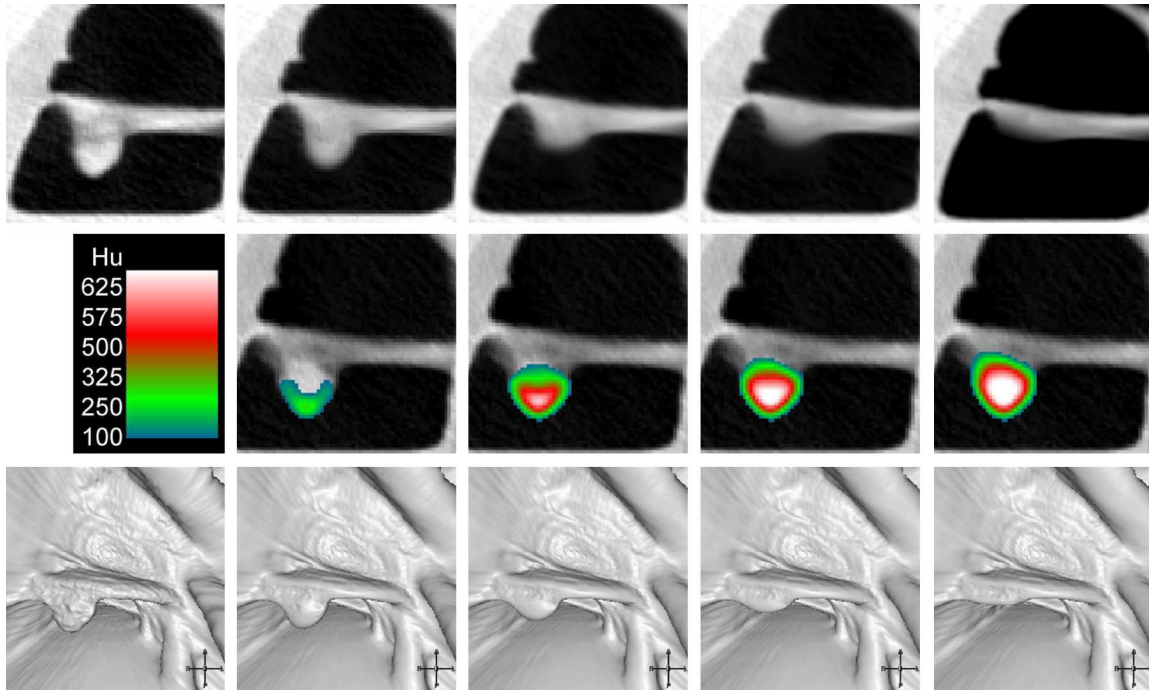


Fig. 7. Polyp (10 mm) at different stages of the intensity deformation [after 0, 10, 40, 80, and 160 iterations of (9)]. First row: original data; second row: overlay showing the intensity changes larger than 100 HU (the color scale was truncated at 650 HU; third row: isosurface renderings (at -650 HU).

[44]. Complementary, the remaining features (MaxIntChange, LongAxis, ShortAxis) relate to size and are directly used to order the candidates. The ranking of the candidates imposes that changes in the decision boundary affects the classification in an ordered fashion.

It may be expected that far more small candidates are detected than large ones due to noise and the small “effective” scale on small objects. Consider a connected number of pixels affected by positively signed noise. Such coherent regions may mimic small objects with positive principal curvature. The derivatives computed from the $3 \times 3 \times 3$ Taylor’s expansion experience a small amount of regularization. Consequently, the little blurring may leave small noise protrusions on an otherwise smooth surface. This is confirmed by the distribution of the false positive candidates with respect to the MaxIntChange feature, which resembles an exponential distribution. Concurrently, we have observed that the polyps denoted by black dots in 6 are approximately uniformly distributed. Therefore, the ratio of the posterior probabilities must follow an exponential decay as a function of MaxIntChange. This is a situation in which a logistic classifier [45] is optimal.

The linear logistic classifier involves estimating the posterior probabilities $p(\omega_i|x)$ instead of the class distributions $p(x|\omega_i)$. These posterior distributions are assumed to be the sigmoidal functions. This is a valid assumption when the classes are Gaussian distributed, or, as in our case, one of the class distributions is exponentially decreasing, while the other is more or less uniformly distributed. A maximum likelihood estimation is performed to find the linear direction in the data that best fits these assumed sigmoidal distribution functions. Using the posterior probabilities instead of the class-dependent

distribution functions makes this classifier less sensitive to the large class imbalance.

As such, the problem is treated as a regression problem rather than a traditional two-class pattern recognition task. In other words, one searches for a linear direction in which the sigmoidal pdfs best describe the data. The performance of the classifier will be assessed by a five-fold, 10 times repeated cross validation (see below).

III. EXPERIMENTS AND RESULTS

The proposed method is applied to the detection of colonic polyps in CT colonography data of 84 patients (see above). We will first show qualitative results. The sensitivity and specificity of the candidate detection step of the CAD system will be given for varying thresholds on the MaxIntChange feature. The results of the complete CAD system after classifier training will be given at the end of this section. We will include the results obtained by the method that involves an explicit (mesh) representation of the colon surface [32] for comparison. The FROC curves were calculated from a leave-one-patient out cross-validation. A polyp was counted as a true positive CAD detection if it was found in at least one of the two scanned positions (prone or supine).

The mean computation time per patient on a PC with a Pentium 4 processor (3.0 GHz) and 2 GB memory was 4 min.

A. Qualitative Analysis

Fig. 7 illustrates how the intensities are modified during the deformation process and how this affects the position of the iso-surface. The first row of grey valued images show cross sections through the polyp after 0, 10, 40, 80, and 160 iterations of (9).

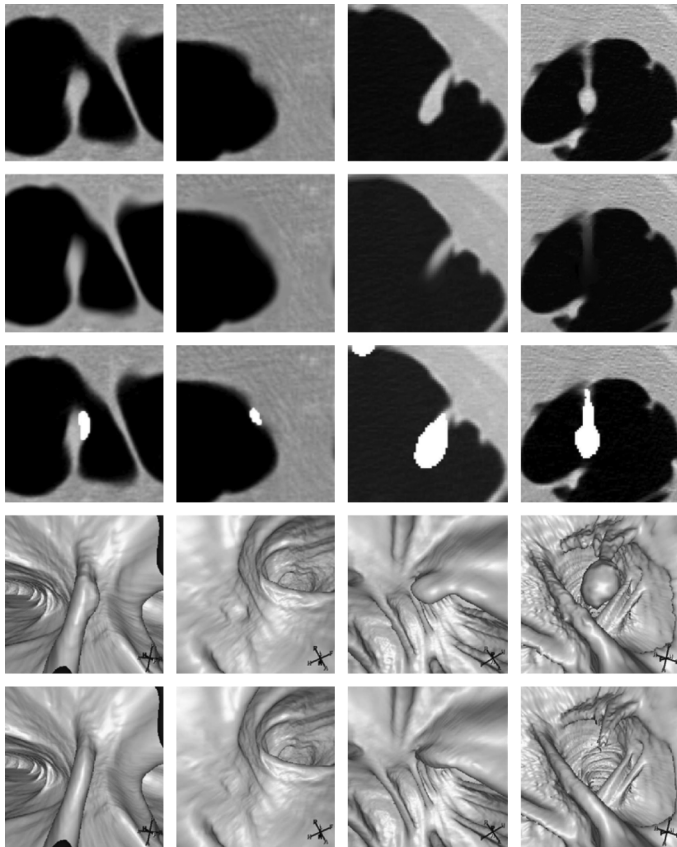


Fig. 8. Typical results for four polyps. Each column shows the results for a different polyp. The first two rows show grey value cross sections before and after intensity deformation. The third row shows the segmentation masks which are obtained by thresholding the intensity change at a level of 100 HU. The last two rows show isosurface renderings (at -650 HU) of the polyps before and after intensity deformation.

The second row shows images with an overlay of a color map of the intensity change for voxels with a change of more than 100 HU. The color bar gives an indication of the amount of change in the polyp compared to its surroundings (< 100 HU; the scale of the color bar was truncated at 650 HU). To appreciate the three dimensional structure, the last row shows isosurface renderings (at -650 HU) that clearly show the gradual deformation of the polyp, while its surroundings stay almost unaltered.

Fig. 8 shows the final outcome for a number of other polyps. The first two rows show grey-valued cross sections, respectively, before and after the intensity deformation. The third row shows an overlay of the segmentation as obtained by thresholding the intensity change between the images in the first two rows at a level of 100 HU. The bottom two rows show isosurface renderings (at -650 HU) of the polyps before and after the deformation. The images demonstrate that the intensity deformation method yields probable estimates of the colon surface. This even applies to objects situated in highly structured surroundings, such as the polyp in the first column. The second column shows the result for a 6 mm polyp. It is situated on an almost flat background. The isosurface rendering containing the colon surface after deformation shows hardly any residual protrusion. The third column displays an elongated polyp on a strongly

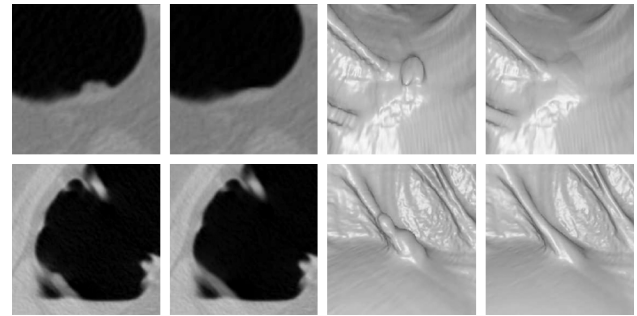


Fig. 9. Each row shows a false positive. First row: Example of stool. Air inside object is clearly visible on first image. Second row: Stool on a fold. The original data is shown in the first and third column. The data after deformation by curvature flow is shown in columns two and four.

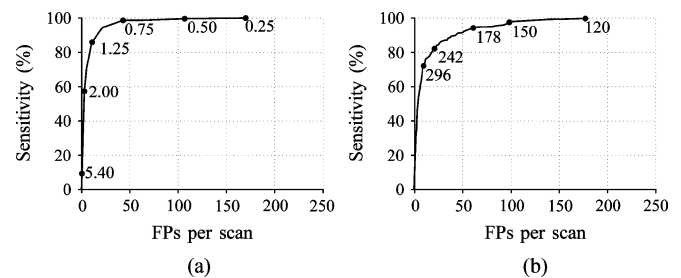


Fig. 10. FROC curves showing the candidate detection sensitivity versus the number of false positives for (a) mesh based and (b) currently proposed technique. The numbers in (a) denote the threshold on the deformation field in mm and in (b) the threshold on the intensity change field in HU.

folded part of the colon. After deformation some residual protrusion can still be observed, albeit small compared to the original protrusion. The same holds for the polyp in the fourth column. This is a classical pedunculated polyp on a narrow stem. The head region is removed, while the stem remains.

Approximately 60% of the false positives are stool and 30% of the false positives are on folds. Among the remaining false positives are detections on the illeocecal valve. All these objects had a shape and structure that closely resemble a polyp (two examples are contained in Fig. 9).

B. Performance of the Candidate Detection

Fig. 10 serves to show that our choice of thresholds is not affecting the detection sensitivity. Both figures (a and b) contain a free-response receiver operating characteristic (FROC) curve for the candidate detection step. Fig. 10(a) was obtained using the method that involves an explicit (mesh) representation of the colon surface [32] and Fig. 10(b) was based on the method presented in the current paper. The independent variable along the curves is the threshold on the displacement of the mesh, respectively the intensity change. In either case a lower threshold returns more candidate objects. Reversely, as the threshold is increased, fewer candidates are found, but also some polyps may be missed. For the full CAD system (see below) we have chosen a threshold for which at least 100% sensitivity is achieved on an independent training set. For the mesh based method this resulted in a threshold of 0.4 mm displacement. For the intensity deformation method we use a threshold of 100 HU on the intensity change. The smaller number of false positives of

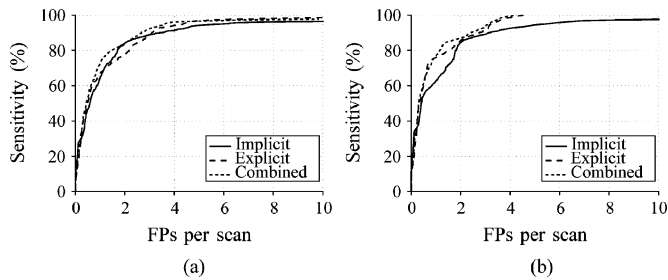


Fig. 11. FROC curves depicting the performance of classification for the mesh based (explicit) and the currently proposed (implicit) technique. The FROC curves were computed by a five times repeated ten-fold cross-validation (a) polyps ≥ 6 mm and (b) polyps ≥ 10 mm.

the mesh representation is due its description by fewer points (about 500 000) than the implicit representation (about 10 million points). Notice that the large number of false positives at this stage is irrelevant: the system's performance is really determined after classifying the candidates (see below).

C. Results After Classification

Fig. 11 shows the overall performance of both the proposed and the mesh based method [32]. The figure shows the performance for the detection of polyps for two size ranges: larger than or equal to 6 mm (including those larger than 10 mm), and larger than or equal to 10 mm. Apparently, the performance of the two methods is comparable. Both techniques perform better on the larger polyps. A sensitivity of 95% for polyps ≥ 6 mm is achieved at an average false positive rate of 4–6 per scan. For polyps ≥ 10 mm, a sensitivity of 95% is obtained at about four false positives per scan.

For our data, approximately 50% of the false positives are stool and 40% are on folds. Among the remaining false positives are detections on the illeocecal valve. All these objects have a shape and internal structure that closely resemble a polyp (two examples are contained in Fig. 11).

D. Combined Approach

In practice we found that particularly the false detections of both methods were to some extent uncorrelated. For instance, the mesh based method typically had false detections emanating from the partial volume effect (PVE) as it operates on a single isophote, whereas the current method was more robust because it took the full transition (air-tissue) into account. Reversely, the current method is inherently sensitive to intensity variations within tissue, especially in thin folds, whereas such problems are excluded in the mesh based method in which feature measurement is confined to the isosurface.

The two methods were combined as follows. The location of the candidates of both methods were compared. A consensus voting was used to accept candidates only if an overlapping candidate was found by the other method, in which case they were linked. Candidates with a vote from only one method were discarded. Fig. 12 confirms that there is complementary information in the two methods. It contains a scatter plot of the MaxIntChange feature versus the maximum displacement of the mesh as obtained by the mesh based method. It can be seen that these correlate well for polyps (black dots). Two regions

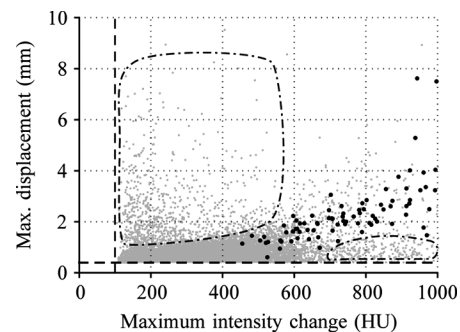


Fig. 12. Feature space of the maximum displacement (explicit method) versus the maximum intensity change (implicit method). The black dots correspond to polyps and the grey dots to false detections. Two regions (encircled by dash-dotted lines top-left and bottom-right) with false detections (grey dots) can be observed in which the depicted features are uncorrelated and complementary.

with false detections (grey dots) can also be observed in which the depicted features are uncorrelated (top-left and bottom-right in both graphs). One region has rather low MaxIntChange, but concurrently quite large maximum displacement of the mesh; another region is characterized by a large MaxIntChange, but a low maximum mesh displacement.

Fig. 11 also contains an FROC curve of the combined approach. It demonstrates improved performance by exploiting the complementary aspects of the two approaches particularly on polyps ≥ 6 mm.

IV. DISCUSSION/CONCLUSION

A novel method was presented which detects polyps based on their protruding character irrespective of the actual shape. The method modifies image intensities at locations of protruding objects. This is achieved by finding a steady state solution of a nonlinear PDE with the recorded image as input. We showed that the intensity change relates to the displacement of iso-contours. We also demonstrated how this relation is made invariant to the anisotropic resolution and sampling of the scanner. This allows for a simple segmentation of polyp candidates by applying a single threshold on the intensity change field. We proposed a measure for the detection of polyp candidates, which directly relates to polyp size, and not to polyp shape. This measure orders detected structures according to size which, in effect, keeps increasingly larger objects further away from the decision boundary. In other words, this limits the risk of missing large polyps. Also, our method does not make a specific choice for the scale for the computation of the first- and second-order derivative operators. The iterative character of the method changes the intrinsic scale of the image (local and anisotropic): the aperture of observation (window size of the operation times the number of iterations) inherently increases.

We have chosen to adapt the convergence criteria of the posed PDE to the local data. Effectively, the deformation of a region stops when it does not expand anymore. This yields a stopping criterion which is data dependent and does not need user interaction. However, the criterion is rather strict as can be seen from Fig. 8 (third column), in which case the protrusion was not completely removed. A high noise level might prevent the algorithm from segmenting the entire polyp area. The (second-

order) Taylor expansion in a $3 \times 3 \times 3$ neighborhood will effectively deal with the noise practically encountered in low-dose (20 mAs) scans.

The method's performance on so-called flat polyps requires further research.

REFERENCES

- [1] E. Konukoglu and B. Acar, "HDF: Heat diffusion fields for polyp detection in CT colonography," *Signal Process.*, vol. 87, no. 10, pp. 2407–16, 2007.
- [2] J. Näppi and H. Yoshida, "Fully automated three-dimensional detection of polyps in fecal-tagging CT colonography," *Acad. Radiol.*, vol. 14, no. 3, pp. 287–300, 2007.
- [3] G. Kiss, J. van Cleynenbreugel, S. Drisis, D. Bielen, G. Marchal, and P. Suetens, "Computer-aided detection for low-dose CT colonography," *Proc. MICCAI'05*, vol. LNCS 3749, pp. 859–67, 2005.
- [4] K. Suzuki, H. Yoshida, J. Näppi, S. Armato, and A. Dachman, "Mixture of expert 3D massive-training ANNs for reduction of multiple types of false positives in CAD for detection of polyps in CT colonography," *Med. Phys.*, vol. 35, no. 2, pp. 694–703, 2008.
- [5] S. Wang, J. Yao, and R. Summers, "Improved classifier for computer-aided polyp detection in CT colonography by nonlinear dimensionality reduction," *Med. Phys.*, vol. 35, no. 4, pp. 1377–86, 2008.
- [6] T. Chowdhury, P. Whelan, and O. Ghita, "A fully automatic CAD-CTC system based on curvature analysis for standard and low-dose CT data," *IEEE Trans. Biomed. Eng.*, vol. 55, no. 3, pp. 888–901, Mar. 2008.
- [7] R. M. Summers, J. Yao, P. J. Pickhardt, M. Franaszek, I. Bitter, D. Brickman, V. Krishna, and J. R. Choi, "Computed tomographic virtual colonoscopy computer-aided polyp detection in a screening population," *Gastroenterology*, vol. 129, no. 6, pp. 1832–44, 2005.
- [8] A. K. Jerebko, J. D. Malley, M. Franaszek, and R. M. Summers, "Support vector machines committee classification method for computer-aided polyp detection in CT colonography," *Acad. Radiol.*, vol. 12, no. 4, pp. 479–86, 2005.
- [9] J. Yao, S. Campbell, A. K. Hara, and R. M. Summers, "Progressive feature vector selection scheme for computer-aided colonic polyp detection," in *Proc. RSNA Scientific Assembly Annu. Meeting Program*, 2004, p. 633.
- [10] P. M. Calvert and H. Frucht, "The genetics of colorectal cancer," *Ann. Intern. Med.*, vol. 137, pp. 603–12, 2000.
- [11] R. M. Soetikno, T. Kaltenbach, R. V. Rouse, W. Park, A. Maheshwari, T. Sato, S. Matsui, and S. Friedland, "Prevalence of nonpolypoid (flat and depressed) colorectal neoplasms in asymptomatic and symptomatic adults," *J. Am. Med. Assoc.*, vol. 299, no. 9, pp. 1027–35, 2008.
- [12] E. Gorgun and J. Church, "Flat adenomas of the large bowel: A single endoscopist study," *Diseases Colon Rectum*, vol. 52, no. 5, pp. 972–972, 2009.
- [13] R. M. Summers, C. D. Johnson, L. M. Pusanik, J. D. Malley, A. M. Youssef, and J. E. Reed, "Automated polyp detection at CT colonography: Feasibility assessment in a human population," *Radiology*, vol. 219, no. 1, pp. 51–9, 2001.
- [14] H. Yoshida and J. Näppi, "Three-dimensional computer-aided diagnosis scheme for detection of colonic polyps," *IEEE Trans. Med. Imag.*, vol. 20, no. 12, pp. 1261–1274, Dec. 2001.
- [15] V. F. van Ravesteijn, C. van Wijk, F. M. Vos, R. Truyen, J. F. Peters, J. Stoker, and L. J. van Vliet, "Computer aided detection of polyps in CT colonography using logistic regression," *IEEE Trans. Med. Imag.*, to be published.
- [16] R. M. Summers, W. S. Selbie, J. D. Malley, L. M. Pusanik, A. J. Dwyer, N. A. Courcoutsakis, D. J. Shaw, D. E. Kleiner, M. C. Sneller, C. A. Langford, S. M. Holland, and J. H. Shelhamer, "Polypoid lesions of airways: Early experience with computer-assisted detection by using virtual bronchoscopy and surface curvature," *Radiology*, vol. 208, no. 2, pp. 331–7, 1998.
- [17] J. Yao, M. Miller, M. Franaszek, and R. M. Summers, "Colonic polyp segmentation in CT colonography—based on fuzzy clustering and deformable models," *IEEE Trans. Med. Imag.*, vol. 23, no. 11, pp. 1344–1352, Nov. 2004.
- [18] E. Konukoglu, B. Acar, S. Paik, F. C. Beaulieu, J. Rosenberg, and S. Napel, "Polyp enhancing level set evolution of colon wall: Method and pilot study," *IEEE Trans. Med. Imag.*, vol. 26, no. 12, pp. 1649–1656, Dec. 2007.
- [19] D. S. Paik, C. F. Beaulieu, G. D. Rubin, B. Acar, R. B. Jeffrey, Jr, J. Yee, J. Dey, and S. Napel, "Surface normal overlap: A computer-aided detection algorithm with application to colonic polyps and lung nodules in helical CT," *IEEE Trans. Med. Imag.*, vol. 23, no. 6, pp. 661–675, Jun. 2004.
- [20] S. B. Göktürk, C. Tomasi, B. Acar, D. S. Paik, C. F. Beaulieu, and S. Napel, "A learning method for automated polyp detection," *Proc. MICCAI'01*, vol. LNCS 2208, pp. 85–93, 2001.
- [21] C. van Wijk, J. Florie, C. Y. Nio, E. Dekker, A. H. de Vries, H. W. Venema, L. J. van Vliet, J. Stoker, and F. M. Vos, "Protrusion method for automated estimation of polyp size on CT colonography," *Am. J. Roentgenol.*, vol. 190, no. 5, pp. 1279–85, 2008.
- [22] B. Acar, C. F. Beaulieu, S. B. Göktürk, C. Tomasi, D. S. Paik, R. B. Jeffrey, Jr, J. Yee, and S. Napel, "Edge displacement field-based classification for improved detection of polyps in CT colonography," *IEEE Trans. Med. Imag.*, vol. 21, no. 12, pp. 1461–1467, Dec. 2002.
- [23] J. J. Dijkers, C. van Wijk, F. M. Vos, J. Florie, Y. C. Nio, H. W. Venema, R. Truyen, and L. J. van Vliet, "Segmentation and size measurement of polyps in CT colonography," in *Proc. MICCAI'05*, 2005, vol. LNCS 3749, pp. 712–9.
- [24] P. Sundaram, A. Zomorodian, C. Beaulieu, and S. Napel, "Colon polyp detection using smoothed shape operators: Preliminary results," *Med. Imag. Anal.*, vol. 12, no. 2, pp. 99–119, 2008.
- [25] J. Liu, J. Yao, and R. Summers, "Scale-based scatter correction for computer-aided polyp detection in CT colonography," *Med. Phys.*, vol. 35, no. 12, pp. 5664–5671, 2008.
- [26] A. Douiri, M. Siddique, X. Ye, G. Beddoe, and G. Slabaugh, "Enhanced detection in CT colonography using adaptive diffusion filtering," *Proc. SPIE*, vol. 7259, p. 23, 2009.
- [27] S. Halligan, S. A. Taylor, J. Dehmeshki, H. Amin, X. Ye, J. Tsang, and M. E. Roddie, "Computer-assisted detection for CT colonography: External validation," *Clin. Radiol.*, vol. 61, no. 9, pp. 758–63, 2006.
- [28] P. Cathier, S. Periaswamy, A. K. Jerebko, M. Dundar, J. Liang, G. Fung, J. Stoeckel, T. Venkata, R. Amara, A. Krishnan, R. B. Rao, A. Gupta, E. Vega, S. Laks, A. Megibow, M. Macari, and L. Bogoni, "CAD for polyp detection: An invaluable tool to meet the increasing need for colon-cancer screening," in *Proc. CARS'04*, 2004, vol. 1268, pp. 978–82.
- [29] S. Taylor, R. Greenhalgh, R. Ilangovan, E. Tam, V. Sahni, D. Burling, J. Zhang, P. Bassett, P. Pickhardt, and S. Halligan, "CT colonography and computer-aided detection: Effect of false-positive results on reader specificity and reading efficiency in a low-prevalence screening population," *Radiology*, vol. 247, no. 1, pp. 133–40, 2008.
- [30] R. Summers, L. Handwerker, P. Pickhardt, R. Van Uitert, S. Y. J. Deshpande, K. K. Deshpande, S. Yeshwant, and M. Franaszek, "Performance of a previously validated CT colonography computer-aided detection system in a new patient population," *Am. J. Roentgenol.*, vol. 191, no. 1, pp. 168–74, 2008.
- [31] N. Petrick, M. Haider, R. Summers, S. Yeshwant, L. Brown, E. Iuliano, A. Louie, J. Choi, and P. Pickhardt, "CT colonography with computer-aided detection as a second reader: Observer performance study," *Radiology*, vol. 247, no. 1, pp. 148–56, 2008.
- [32] C. van Wijk, V. F. van Ravesteijn, F. M. Vos, R. Truyen, A. H. de Vries, J. Stoker, and L. J. van Vliet, "Detection of protrusions in curved folded surfaces applied to automated polyp detection in CT colonography," *Proc. MICCAI'06*, vol. LNCS 4191, pp. 471–8, 2006.
- [33] R. E. Van Gelder, C. Y. Nio, J. Florie, J. F. Bartelsman, P. Snel, S. W. De Jager, S. J. Van Deventer, J. S. Lameris, P. M. M. Bossuyt, and J. Stoker, "Computed tomographic colonography compared with colonoscopy in patients at increased risk for colorectal cancer," *Gastroenterology*, vol. 127, no. 1, pp. 41–8, 2004.
- [34] W. J. Niessen, B. M. ter Haar Romeny, L. M. J. Florack, and M. A. Viergever, "A general framework for geometry-driven evolution equations," *Int. J. Comput. Vis.*, vol. 21, no. 3, pp. 187–205, 1997.
- [35] L. J. van Vliet and P. W. Verbeek, "Curvature and bending energy in digitized 2D and 3D images," in *Proc. 8th Scandinavian Conf. Image Anal.*, 1993, pp. 1403–10.
- [36] P. J. Olver, G. Sapiro, and A. Tannenbaum, "Invariant geometric evolutions of surfaces and volumetric smoothing," *SIAM J. Appl. Math.*, vol. 57, no. 1, pp. 176–94, 1997.
- [37] G. Huisken, "Flow by mean curvature of convex hypersurfaces into spheres," *J. Differ. Geom.*, vol. 20, pp. 237–68, 1984.
- [38] K. A. Brakke, "The motion of a surface by its mean curvature," Ph.D. dissertation, Princeton Univ., Princeton, NJ, 1978.
- [39] H. Scharr, "Optimal operators in digital image processing," Ph.D. dissertation, Ruprecht-Karls-Universität Heidelberg, Heidelberg, Germany, 2000.

- [40] J. P. Thirion and A. Gourdon, "Computing the differential characteristics of iso-intensity surfaces," *Comput. Vis. Image Understand.*, vol. 61, no. 2, pp. 190–202, 1995.
- [41] J. van Kan, A. Segal, and F. Vermolen, *Numerical Methods in Scientific Computing*, 1st ed. Delft, The Netherlands: VSSD, 2005.
- [42] W. Ames, *Nonlinear Partial Differential Equations in Engineering*. New York: Academic, 1972, vol. 1.
- [43] I. W. O. Serlie, *CT Imaging Characteristics* Delft Univ. Technol., Delft, The Netherlands, Tech. Rep. QI-2006-01, 2006, Tech. Rep. QI-2006-01.
- [44] D. M. J. Tax, "One-Class Classification," Ph. D, Delft Univ. Technol., Delft, The Netherlands, 2000.
- [45] A. R. Webb, *Statistical Pattern Recognition*, 2nd ed. New York: Wiley, 2002.